Original Article

Journal of Tissue Engineering
Volume 15: 1–18

DOI: 10.1177/20417314231219280
journals.sagepub.com/home/tej
Sage

Mesenchymal stem cells overexpressing XIST induce macrophage M2 polarization and improve neural stem cell homeostatic microenvironment, alleviating spinal cord injury

Dan Zhu[1*], Tie Peng[2*], Zhenwang Zhang[1*], Shuang Guo[1*], Ying Su[2], Kangwei Zhang[2], Jiawei Wang[1] and Chao Liu[1]

Abstract

Spinal cord injury (SCI) is a significant cause of disability worldwide, with limited treatment options. This study investigated the potential of bone marrow-derived mesenchymal stem cells (BMSCs) modified with XIST lentiviral vector to modulate macrophage polarization and affect neural stem cell (NSC) microenvironment reconstruction following SCI. Bioinformatics analysis revealed that MID1 might be crucial for BMSCs' treatment of SCI. XIST overexpression enriched Zmynd8 to the promoter region of MID1 and inhibited MID1 transcription, which promoted macrophage M2 polarization. In vitro experiments showed that BMSCs-XIST promoted NSC proliferation, migration, differentiation, and axonal growth by inducing macrophage M2 polarization, suppressing inflammation, and accelerating the re-establishment of the homeostatic microenvironment of NSCs. In vivo, animal experiments confirmed that BMSCs-XIST significantly alleviated SCI by promoting NSC differentiation and axon formation in the injured area. The study demonstrated the potential of XIST-overexpressing BMSCs for treating SCI by regulating macrophage polarization and homeostasis of the NSC microenvironment. These findings provide new insights into the development of stem cell-based therapies for SCI.

Keywords

Spinal cord injury, bone marrow mesenchymal stem cells, neural stem cells, XIST, MID1, M2 type macrophage polarization, neuronal differentiation, homeostatic microenvironment remodeling

Date received: 5 July 2023; accepted: 22 November 2023

Introduction

Spinal cord injury (SCI) is a severe chronic disease that burdens patients significantly physically and emotionally.[1] Unfortunately, there is no fully effective treatment.[2] Neural stem cells (NSCs) have the potential to repair damaged neural tissues and have, therefore, become the focus of research for SCI treatment.[3] However, alterations in the tissue environment after SCI, such as inflammation and immune response, hinder the growth and differentiation of NSCs and, thus, the repair of neural injury.[4]

M1 macrophages secrete pro-inflammatory cytokines such as interleukin-β (IL-β), tumor necrosis factor-α (TNF-α), IL-6, and interferon-γ (IFN-γ), which exacerbate spinal cord injuries (SCIs). On the other hand, M2 macrophages secrete anti-inflammatory cytokines, such as

[1]Hubei Key Laboratory of Diabetes and Angiopathy, Xianning Medical College, Hubei University of Science and Technology, Xianning, P.R. China
[2]Xianning Medical College, Hubei University of Science and Technology, Xianning, P.R. China

*These authors are regarded as co-first authors.

Corresponding author:
Chao Liu, Hubei Key Laboratory of Diabetes and Angiopathy, Xianning Medical College, Hubei University of Science and Technology, No. 88, Xianning Avenue, Xianan District, Xianning, Hubei Province 437100, P.R. China.
Email: liu_chao@hbust.edu.cn

IL-4, IL-10, IL-13, and neurotrophic factors, to inhibit inflammation and neuronal apoptosis. Therefore, modulation of macrophage phenotypes to promote SCI repair represents a promising therapeutic target.[5] Furthermore, studies have indicated that post-SCI angiogenesis is a crucial step in tissue repair and is closely related to neuronal regeneration. Peptide modification with nerve peptide substance P of self-assembling RADA16 effectively stimulates angiogenesis in the injured spinal cord.[6] Another study revealed the utility of hyaluronic acid (HA) in promoting axonal regeneration and angiogenesis. It was observed that severed axons in the injured site of mouse spinal cords extended into transplanted HA-based hydrogels.[7]

The XIST (X inactive specific transcript) gene is a long non-coding RNA that is found mainly on the single X chromosome in females and plays a vital role in the maintenance of the single X chromosome, balancing the number of sex chromosomes by suppressing the expression of related genes on the single X chromosome. In addition, the XIST gene also has various biological functions, such as regulating cell signaling, inducing cell differentiation, and regulating the immune system.[5] In particular, XIST gene expression can affect macrophage polarization and, thus, the immune system response.[8]

Recent studies have shown that the XIST gene may be associated with the progression of spinal cord injury.[9] The expression level of the XIST gene was significantly increased after spinal cord injury and correlated with the severity of spinal cord injury and apoptosis of neurons and glial cells.[10] In addition, it was also found that the survival and regeneration of neurons and glial cells after spinal cord injury could be affected by regulating the expression levels of XIST genes, suggesting that XIST genes may be involved in the inflammatory response and apoptotic process after spinal cord injury, which in turn affects the progression and repair of injury.[9] Furthermore, the expression level of the XIST gene is higher in MSCs because these cells are undifferentiated stem cells, which are required to maintain the X chromosome in an activated state.[11] In addition, modulation of XIST gene expression levels can reduce the differentiation level of MSCs.[12]

Post-spinal cord injury, the inflammatory response becomes the main microenvironment at the injury site, while the polarization state of macrophages determines the cytokine milieu within the injured area. M2 macrophages, known to produce high levels of anti-inflammatory factors such as IL-10 and TGF-β,[13] play a crucial role in tissue repair and promoting axonal regeneration. Macrophage numbers increase significantly at 3 and 7 days after SCI injury, while macrophage-mediated inflammatory responses peak approximately 7 days after injury and slow functional recovery in patients. Macrophages can also produce growth factors that promote angiogenesis, stimulate fibroblast proliferation, and regulate connective tissue synthesis, critical factors in tissue repair.[14] The main difference between the different roles of macrophages on the prognosis of SCI injury lies in the different sources of macrophages.[15] It has been demonstrated that knockdown of XIST can regulate miR-27a/Smurf1 axis to reduce apoptosis of microglia and attenuate inflammatory injury in mouse SCI model.[10] In addition, the knockdown of XIST acts on M1 macrophages, affecting co-cultured chondrocytes' apoptosis.[16] XIST promotes burn healing by targeting IL-33 to M2 macrophages via miR-19b.[17]

This study aims to investigate how XIST overexpression lentiviral vector affects BMSCs to regulate macrophage M2 polarization and thus impacts the reconstruction of the NSC microenvironment in SCI. Our study will provide insight into the mechanism of SCI development and provide a new strategy for treating SCI, which will provide strong support for future research efforts and thus bring more help to SCI patients with crucial scientific value and clinical significance.

Materials and methods

SCI-related microarray data download and differential gene screening

Download spinal cord injury (SCI)-related datasets GSE180767 and GSE132242 from the Gene Expression Omnibus (GEO) database (http://www.ncbi.nlm.nih.gov/geo/), where three Sham group and three SCI group mouse spinal cord samples were selected from the GSE180767 dataset, and four Sham group and four SCI group mouse spinal cord samples were selected from the GSE132242 dataset. SCI group mice spinal cord samples selected GSE132242 data set four Sham group and four SCI group mice spinal cord samples; download BMSCs transplantation for spinal cord injury-related data sets GSE139227, GSE178564, GSE125176, of which, selected GSE139227 data set three SCI group and six SCI + BMSCs group mouse spinal cord samples, selected GSE178564 dataset nine SCI group and ten SCI + BMSCs group mouse spinal cord samples, selected GSE125176 dataset eight Sham group and eight SCI group BMSCs samples.

The GSE180767 and GSE132242 data sets were merged using the "limma" and "sva" packages and then batch-corrected. After correction, the merged data were evaluated by visualizing PCA plots using the "ggplot2" package.[18–20] In addition, we also merged GSE139227 and GSE178564 with batch correction for subsequent analysis.

Public data immune infiltration analysis

The expression matrix of 22 immune cell signature gene sets was downloaded from the CIBERSORT website (https://cibersort.stanford.edu/), and immune cells in the

combined data of GSE180767 and GSE132242 were analyzed by the CIBERSORT algorithm with 1000 simulations, and immune cells without infiltration were excluded. In addition, the relationship between target genes and different immune cells was examined by the "CIBERSORT" R script to analyze the correlation between core gene expression and SCI immune cell infiltration.[21]

The co-expression network was constructed by the R software package "WGCNA." The workflow included gene co-expression network construction, module identification, module relationship analysis, and identification of highly correlated genes. The soft threshold parameter $\beta = 11$ and the scale-free $R^2 = 0.90$ were set to obtain the most significantly positively correlated module genes with SCI for subsequent analysis.[22,23]

Public data differential expression gene acquisition

We analyzed differential gene expression on the merged data using the "limma" package in the R programming language. Genes with $|\log FC| > 1$ and p-value<0.05 were selected as differentially expressed genes (DEGs). The R programming language generated a volcano plot of the differential genes.

Functional and gene enrichment analysis of differentially expressed genes

GO enrichment analysis and KEGG enrichment analysis of differentially expressed genes were performed using the R language "ClusterProfiler" package, in which GO enrichment analysis included biological process (BP), molecular function (MF), and cellular component (CC) analysis. Therefore, GO enrichment analysis included biological process (BP), molecular function (MF), and cellular component (CC) analysis, and $p < 0.05$ was used as the screening condition.

Machine learning to construct LASSO regression models to screen for signature genes

Regression analysis of sequenced differentially expressed genes was performed using the R language "glmnet" package to screen for the core signature gene of M2 macrophage polarization.[24] The regulatory relationship between lncRNA and core signature genes in BMSCs was predicted by the catRAPID website (http://service.tartaglialab.com/page/catrapid_omics2_group).

Identification of BMSCs

Well-grown mouse BMSCs (Item No. CP-M131, Procell, China) were taken from BMSCs in α-MEM (SH30265.01, HyClone, Thermo Fisher Scientific, USA) supplemented with 15% fetal bovine serum (FBS; 10091148, Thermo Fisher Scientific, USA) and 100 U/mL penicillin-streptomycin solution (10378016, Thermo Fisher Scientific, USA) in α-MEM (SH30265.01, HyClone, Thermo Fisher Scientific, USA) medium. BMSCs were passaged when they reached 80% confluence, and third generation BMSCs were used for subsequent experiments.

After washing with PBS, 1×10^6/mL single-cell suspensions were made. Fluorescently labeled antibodies were added in groups: CD44 (ab243894), CD73 (ab288154), CD90 (ab3105), CD105 (ab221675), CD45 (ab10558), and CD31 (ab7388), incubated at 4°C for 30 min and then incubated with The unlabeled antibodies were washed off with PBS after incubation at 4°C for 30 min, and the samples were analyzed by flow cytometric analysis for the expression of the corresponding labeled antibodies, which were purchased from Abcam (UK).

The osteogenic, lipogenic, and chondrogenic differentiation ability of BMSCs was observed with alizarin red, oil red O staining, and Alcian blue staining, respectively, according to the BMSCs Induced Differentiation (Osteogenic, Lipogenic, and Chondrogenic) kit instructions (PD-003/4/5, Procell, China).[25]

Lentiviral construction of stable turnaround BMSCs-XIST

Mouse bone marrow-derived mesenchymal stem cells (BMSCs) were seeded onto a 6-well plate at 2×10^6 cells/healthy density and cultured overnight at 37°C. Overexpressed XIST recombinant lentivirus was added to each well at a final concentration of 1×10^8 TU/mL or lentivirus control containing an empty vector. After 6 h of infection, the medium was replaced with a fresh culture medium. Following a 72-h viral infection, the medium was replaced with a complete culture medium containing 2 μg/mL puromycin for continued culturing for 2 days to select stably transfected cell lines. The XIST recombinant lentivirus was constructed and provided by Shanghai GenePharma Ltd (Shanghai, China) construct.[26]

Culture and identification of NSCs and macrophages

NSCs were isolated from the spinal cords of neonatal C57BL/6N mice (strain code: 213, Beijing Viton Lever Laboratory Animal Co., Ltd., China). After careful peeling of the meninges, the spinal cord tissue was cut into 1 mm^3 slices and digested with TrypLE expression enzyme (12604013, Gibco, USA) for 15 min at 37°C. The trypsin was then diluted with PBS, and the cells were collected by centrifugation at 500*g* for 5 min. Next, the cells were collected and centrifuged at 500*g* for 5 min. Next, the cells were suspended in a serum-free DMEM/F12 medium containing 20 ng/mL bFGF, 20 ng/mL EGF, 1% N2, and 2%

B27. Half of the medium was replaced with fresh medium every 3 days. After 10 days, the newly formed neurospheres were digested into individual NSCs and cultured in an adhesion medium containing 10% fetal bovine serum. The NSCs were cultured in 24-well plates covered with poly-D-lysine overlay, 1×10^5 cells/well. They were then cultured with a neuronal induction medium (NIM). Half of the medium was changed to fresh medium every 2 days. NSCs were observed by ordinary light microscopy, and the purity of NSCs was examined by immunofluorescence co-staining to detect the expression of Nestin and SOX2 in NSCs.[27–29]

Mouse bone marrow-derived macrophages BMDM (CP-M141, Procell, China) were cultured in RPMI-1640 medium containing macrophage colony-stimulating factor (100 ng/mL, R&D Systems, Minneapolis, MN, USA; 11875119, Thermo Fisher Scientific, USA) in To induce BMDM polarization to M1: 20 ng/mL IFN-γ (AF-300-02, Peprotech)/100 ng/mL LPS (916374, Sigma-Aldrich, USA) was added; to induce BMDM polarization to M2: 20 ng/mL IL-4 (SRP4137, Sigma- Aldrich, USA) and incubated for 5, 24 and 48 h; M0-type macrophages, that is, BMDM, were left untreated.

BMSCs-XIST co-cultured with BMDM

The mouse bone marrow-derived macrophages BMDM and mouse BMSCs were co-cultured, the mouse BMDM cells were placed in the upper chamber of Transwell, and the transfected mouse BMSCs cells of each group were placed in the lower chamber of Transwell for 24 h. After co-culture, the BMDM cells were collected for subsequent experiments.[30]

Co-cultivation of M0–M2 macrophages and NSCs in conditioned medium

After stimulating M0, M1, and M2 macrophages for 24 h, the supernatant was removed, and the cells were washed twice with PBS. An equal volume of fresh neural progenitor cell culture medium was added to each macrophage culture medium group, followed by a 24-h incubation period. The supernatant collected from this incubation served as the primary culture medium, to which 100 μg/mL penicillin/streptomycin (15140148, Gibco, USA), 10 mmol/l L-glutamine (21051024, Gibco, USA), 1% N2 (abs9121, Absin), 20 μL/mL B-27 supplement (A3582801, Gibco, USA), EGF (SRP3196, 5 ng/mL, Sigma-Aldrich), and FGF (SRP4057, 5 ng/mL, Sigma-Aldrich) were added. This produced a macrophage-conditioned medium (M0–CM, M1–CM, and M2–CM). NSCs were then cultured in M0–CM, M1–CM, and M2–CM for 7 days, after which the proliferation, migration, differentiation, and axon formation of the NSCs were assessed.[29]

EdU staining and CCK-8 assay to detect the proliferation of NSCs

Cell Counting Kit-8 (40203ES60, Yeasen, Shanghai, China) was used. Briefly, NSCs were cultured with different treatments of the macrophage-conditioned medium, and the proliferation of NSCs was measured on days 1, 3, and 7. After NSCs were cultured in a medium containing CCK8 (1:10) for 3 h, 100 μL of supernatant was transferred to 96-well culture plates. The absorbance of the solution was measured at 450 nm[31,32] using an enzyme marker (EON, Genetics Ltd.). Under the same treatment conditions, the proliferation of NSCs was detected on day 7 using the EdU assay kit (C10310-3, RiboBio, China).

NSCs migration experiment

NSCs were cultured with differently treated macrophage-conditioned medium and incubated at 37°C for 24 h. After that, images of each well were taken using a Leica DMi8 wide-field microscope. The migration index was defined as the total area of migrating cells divided by the internal area of the neurospheres of NSCs. The internal area and total area of the neurosphere were measured using ImageJ software.[33]

Construction of SCI mouse model

Forty-eight C57BL/6N mice (8-week-old, 20–25 g) were purchased from Beijing Viton Lever Laboratory Animal Co., Ltd (strain code: 213, Beijing, China) and housed in separate cages in an SPF-grade animal laboratory at 60%–65% humidity and 22°C–25°C, and provided with free food and water under a 12-h light and dark cycle. The experiments were started after 1 week of acclimatization feeding, and the health status of mice was observed before the experiments. All animal experiments were approved by the Animal Ethics Committee of the Hubei University of Science and Technology (No. 2023-04-004). All animal experiments in this study followed the local management principles and the use of laboratory animals.

A total of four groups were randomly assigned in this study: the Sham group (undergoing surgery without spinal cord transection), the SCI group (undergoing spinal cord transection and receiving an equal volume of PBS injection), the BMSCs group (undergoing spinal cord transection and injected with 3 μL of 2×10^5 BMSCs using a Hamilton syringe as a control), and the BMSCs-XIST group (undergoing spinal cord transection and injected with 3 μL of 2×10^5 BMSCs-XIST using a Hamilton syringe, with the needle tip retained in the spinal cord for 5 min after cell injection).[34] Each group consisted of 12 mice.

SCI surgical procedure. Mice were anesthetized by intraperitoneal injection of a mixture of 70 mg/kg ketamine and

5 mg/kg thiazide. After cessation of the corneal reflex, the surgical site was shaved, the skin was disinfected with a tincture of iodine agent and 70% ethanol, and the skin layer and paravertebral muscle layer of the mouse's back were then incised. After the transection of the spinal cord, a 2 mm segment of the spinal cord was removed entirely by laminectomy at the level of T9–T10. After separate treatments, the paravertebral muscles and skin were closed in layers and disinfected with 70% ethanol. Postoperatively, these mice were placed in warm cages for recovery and given food and water. The weight of the mice was measured before surgery and 6 weeks after surgery.

At 6 weeks postoperatively, subjecting the mice to a 20-min cardiac perfusion with polyformaldehyde, approximately 2 mm of spinal cord tissue was obtained by dissection at the injury site, fixed in 4% paraformaldehyde at 4°C for 24 h, dehydrated with 20% v/v sucrose overnight, and then dehydrated with 30% sucrose at 4°C for an additional 48 h. These dissected tissues were embedded in OCT and cut longitudinally into 10 μm-thick frozen sections using a frozen section machine (Leica CM1950. Germany). Intact, flat, unseparated, and non-folded frozen sections were selected for histological staining and immunofluorescence co-staining.[31,32]

Motor behavior and footprint analysis of mice

The mice were scored weekly on the Basso-Mouse Scale (BMS). The hindlimb movements of four groups of mice were observed in an 80 cm lateral length grid for 6 weeks after surgery. The BMS score was used to assess hindlimb motility, and the level of the BMS score represented the status of recovery of hindlimb motor function in mice with spinal cord injury; the higher the score, the better the recovery, and the score ranged from 0 (no ankle motion) to 9 (full functional recovery). Mice were excluded if their BMS score was higher than 3 at 1 day after injury.

Body weight support and limb coordination were assessed by footprint analysis. First, the forelimbs and hindlimbs of the mice were stained with blue and red ink, respectively. Subsequently, mice were made to walk freely on white paper (1 m long and 7 cm wide), and the distance between the left and right hind paws was used as the basis for assessing weight support; the distance between the center pad of the forelimbs and the vertical center pad of the hind limbs was used to assess limb coordination; and the rotation angle (AR) was the angle formed by the third toe and the two stride lines at the center of the hind paws.[31]

Histological analysis

Spinal cord tissue sections were stained for H&E to detect pathology. Spinal cord tissue was fixed with 4% paraformaldehyde for 12 h. Paraffin-embedded tissue was cut at 5 μm. Slides were rehydrated in graded ethanol, H&E stained, rehydrated in increasing increments and observed with light microscopy at different magnifications. Damaged neurons were counted by assessing gray matter alterations using a 6-point scale: (0) no lesion found; (1) gray matter containing 1–5 eosinophil neurons; (2) gray matter containing 5–10 eosinophil neurons; (3) gray matter containing more than 10 eosinophil neurons; (4) small infarcts, areas of gray matter less than one-third of the area; (5) moderate infarcts, areas of gray matter between areas between one-half and one-third for; and (6) severe infarcts, areas with gray matter area greater than one-half or more. The mean score of each group was recorded to obtain the cumulative scores.[32,35]

Adjacent tissue sections were stained with Masson's trichrome staining kit (G1340, Solarbio, China) to detect collagen tissue deposition within the injury site.

Immunofluorescence co-staining

Tissue sections were permeabilized with 0.5% Triton X-100 in PBS solution and closed with 5% BSA for 1 h. Cells were then fixed with 4% paraformaldehyde at room temperature for 15 min, followed by two washes in PBS and 0.5% Triton X-100 (P0096, Beyotime, China) permeabilized for 10 min. Tissue sections or cells were then mixed with primary antibodies: Rabbit anti-MAP2 (ab183830, 1:500), rabbit anti-GFAP (ab207165, 1:500), rabbit anti-SYN1 (#5297, 1:200, CST, USA), mouse anti-Nestin (ab81462, 1:100), rabbit anti-SOX2 (ab92494, 1:100), rabbit anti-F4/F80 (ab6640, 1:200) were incubated overnight at 4°C. After washing three times with PBS solution. Next, the sections were incubated with Alexa Fluor 488/594-coupled secondary antibodies (A32766/A-21203/A-21206/A32754, 1:500, Thermo Fisher Scientific, USA) for 1 h. Then, the sections were washed three more times with PBS solution and incubated with DAPI The sections were stored at 4°C and then observed with a confocal microscope (Leica SP8).[32] Primary antibodies were purchased from Abcam (UK), except for SYN1.

Detection of M1 and M2 macrophage ratios in mouse spinal cord tissue by flow cytometry

Mouse spinal cord tissue was collected in ice-cold PBS and processed as described. Briefly, samples were mechanically cut using a McIlwain tissue sectioner (Mickle Laboratory Engineering) and then enzymatically digested with 3 mg/mL collagenase type A (Roche) and 25 μg/mL DNase I (Sigma) in serum-free medium in a shaking water bath at 37°C for 1 h. After washing, the samples were treated with fluorescein-coupled antibodies CD11b (PE-Cyanine5, 15-0112-82, eBioscience™, Invitrogen), NOS (Alexa Fluor™ 488, 53-5920-82, eBioscience™, Invitrogen) or CD11b (PE-Cyanine5, 15-0112-82, eBioscience™, Invitrogen), CD206 (Alexa Fluor™ 488,

53-2061-82, eBioscience™, Invitrogen), cells were stained and incubated for 1 h against light, washed once with PBS, and 0.5 mL PBS was used to resuspend the cells. Diva software (BD Biosciences) to collect data on a BD LSRII flow cytometer, and FlowJo software version 9.9.6 was used for data analysis.[36]

ChIP detection of Zmynd8 enrichment in the MID1 promoter region

The cells of each group of BMDM were fixed with formaldehyde for 10 min to produce DNA-protein crosslinks. The ultrasonic fragmentation apparatus was set up to break the chromatin into fragments (200–500 bp) by sonication for 10 s at 10 s intervals for 15 cycles. After the cells were fully lyzed, 10% of the volume of whole cell lysate was taken as input, and the remaining samples were centrifuged at 4 °C at 12,000*g*. The supernatant was collected and divided into two tubes at 10 min. Negative control rabbit IgG (ab171870, Abcam, UK) and Zmynd8 (1:100, Cat No. 11633-1-AP, Proteintech) were added, respectively, and incubated overnight at 4°C to bind fully. Protein and DNA complexes were precipitated with Pierce protein A/G Magnetic Beads (Thermo, 88803), centrifuged at 5000*g* for 1 min, the supernatant discarded, non-specific complexes washed, uncrosslinked overnight at 65°C, and DNA fragments were recovered by phenol/chloroform extraction and purification followed by qRT-PCR to detect changes in MID1 promoter fragment enrichment.[37]

A dual luciferase reporter assay

BMDM cells were cultured in a 48-well plate for 24 h. To construct the MID1 plasmid, the pGL3-promoter (E1761, ProMega Biotech, Beijing, China) luciferase reporter vector was co-transfected with either oe-Zmynd8 or a negative control (oe-NC) plasmid into BMDM cells for 48 h. The Rluc (Renilla luciferase) and Luc (firefly luciferase) fluorescence were measured using the Pierce™ SuperSignal™ Dual-Luciferase Reporter Assay Kit (16186, Thermo Fisher Scientific, USA). Rluc was used as an internal control, and the relative luciferase activity was determined as the ratio of Luc to Rluc fluorescence.[38,39] The experiment was repeated three times.

RT-qPCR

According to the instructions, total tissue or cellular RNA was extracted using a Trizol reagent (15596026, Invitrogen, USA). cDNA was reverse-transcribed from RNA according to the instructions of the PrimeScript RT reagent Kit (RR047A, Takara, Japan). The synthesized cDNA was assayed by Fast SYBR Green PCR kit (11736059, Thermo Fisher Scientific, USA) for RT-qPCR detection, and three replicates were set up for each well. GAPDH was used as an internal reference $2^{-}\Delta\Delta^{Ct}$ Relative expression was calculated.[40–42] The experiment was repeated three times. The primer sequences used for RT-qPCR in our study are shown in Supplemental Table 1, and Takara synthesized the primer sequences.

Western blot

Cellular protein samples isolated from tissue and whole cell lysates were quantified using the Pierce BCA Protein Assay Kit (23227, Thermo Fisher Scientific, USA). Tissue and cellular proteins were extracted using RIPA buffer. About 20 μg of protein from each sample was loaded onto a sodium dodecyl sulfate-polyacrylamide electrophoresis gel and transferred to a nitrocellulose membrane. About 5% skimmed milk powder was used for 1 h after incubation with primary antibodies: rabbit anti-MAP2 (ab281588, 199 kDa, 1:1000), rabbit anti-GFAP (ab33922, 50 kDa, 1:10,000), and rabbit anti-SYN1 (ab274430, 74 kDa, 1:1000), rabbit anti-MID1 (ab70770, 74 kDa, 1:1000), rabbit anti-GAPDH (ab9485, 37 kDa, 1:1000). All antibodies were purchased from Abcam (Cambridge, UK). The following day, secondary anti-goat anti-rabbit IgG H&L (ab6721, 1:5000, UK) was applied for 1 h. Immunoreactive bands were visualized using enhanced chemiluminescence reagent (WP20005, Thermo Fisher Scientific, USA), and ChemiDoc XRS Plus luminescent image analyzer (Bio-Rad Laboratories, Hercules, CA, USA) was used to image the pictures. The groups of bands in the images were quantified in grayscale using Image J analysis software, using GAPDH as an internal reference.[43]

Statistical analysis

Statistical analysis of our study data was performed using the SPSS software package (version 23.0, IBM SPSS) or GraphPad Prism software version 8.0. The measures were expressed as mean ± standard deviation and firstly tested for normality and chi-square, tested for conformity to normal distribution and chi-square, unpaired *t*-test was used between groups, and one-way ANOVA or ANOVA of repeated measures data was used to compare multiple groups. Pearson was used for the correlation analysis of the two indicators. $p < 0.05$, $p < 0.01$, and $p < 0.001$ indicate statistically significant differences.

Results

Significantly increased M1-type macrophage infiltration in SCI samples

Firstly, we merged the SCI-related datasets GSE180767 and GSE132242 for batch correction. As shown in Supplemental Figure 1A and B, before batch correction, there were significant differences between the two

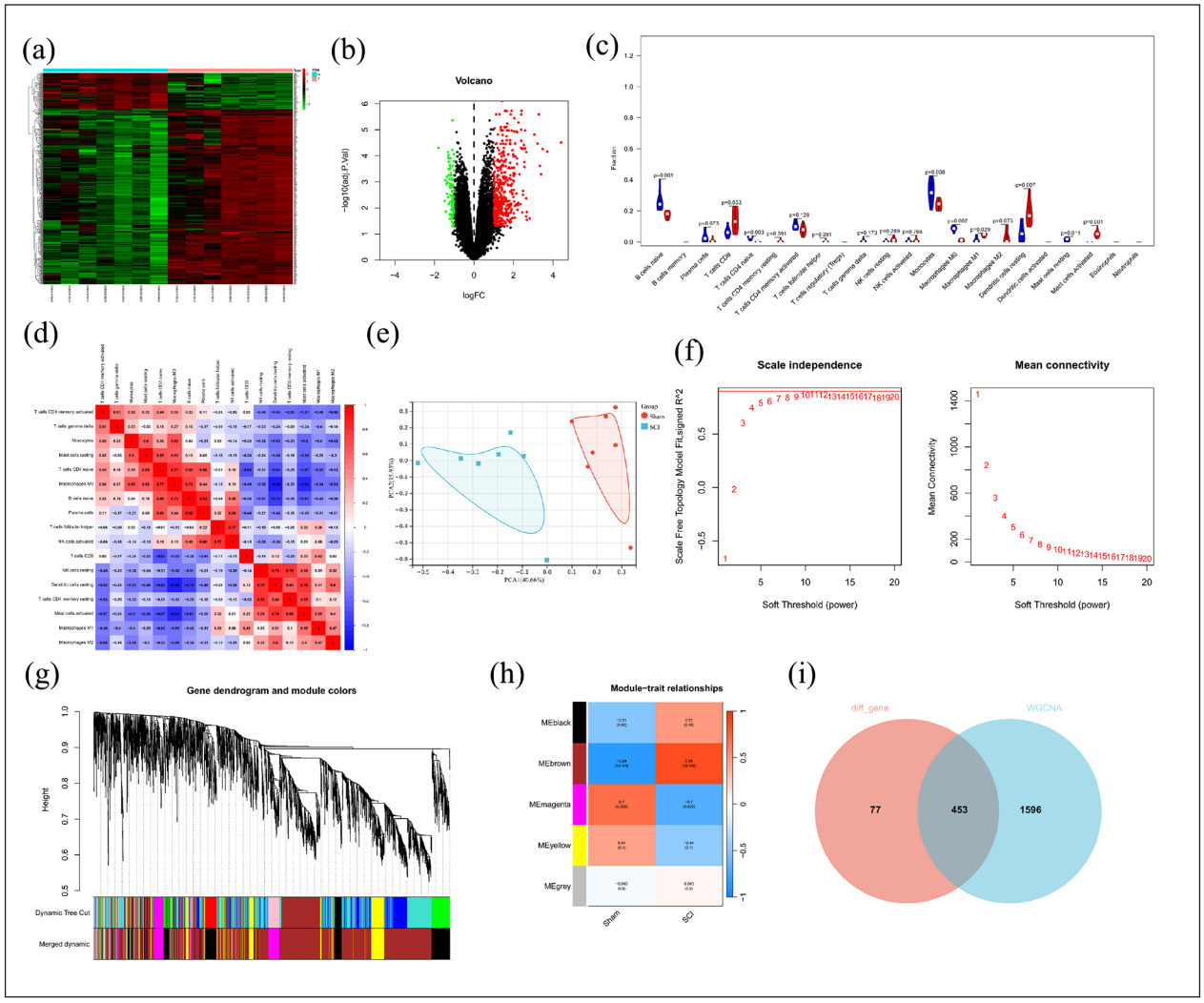

Figure 1. Bioinformatics analysis for the infiltration status of immune cells and inflammation in SCI in the central nervous system. (a) a heatmap illustrating the expression of 530 DEGs in the merged datasets of GSE180767 and GSE132242, (b) a volcano plot illustrating the differential expression of these 530 DEGs in the merged datasets, with black indicating genes with no differential expression, red denoting upregulated genes, and green representing downregulated genes, (c) A violin plot, based on the CIBERSORT algorithm, displays the proportions of 22 immune cell infiltrations in the merged datasets of GSE180767 and GSE132242, with blue and red representing the SCI and Sham groups, respectively, (d) a correlation heatmap of the proportions of immune cell infiltrations in the merged datasets, using the CIBERSORT algorithm, (e) the degree of dispersion of immune cell infiltrations in the SCI and Sham groups in the merged datasets of GSE180767 and GSE132242, as analyzed via PCA. The SCI and Sham groups consist of seven cases each, (f) the analysis of scale-free fitting indices and average connectivities for various soft threshold powers, (g) a gene co-expression network constructed using WGCNA, with each color representing a module within this network, (h) the analysis of the correlation between different modules and diseases, with each cell containing the correlation coefficient and respective *p*-value, and (i) a Venn diagram depicting the overlap between genes in the SCI-associated module (brown) and differentially expressed genes.

datasets. However, after batch correction, the differences became significantly smaller, indicating reduced noise. Subsequently, we performed differential analysis on the batch-corrected mRNA dataset and identified a total of 530 differentially expressed genes (DEGs), with 439 upregulated and 91 downregulated genes (Figure 1(a) and (b)).

Next, we estimated the infiltration of immune cells in the merged dataset using the CIBERSORT algorithm. By plotting heatmaps and bar charts for the infiltration of 22 immune cell types, we observed a significant increase in the proportion of dendritic cells, mast cells, and M1 macrophages after SCI (Figure 1(c), Supplemental Figure 1C). Furthermore, these three cell types showed certain correlations (Figure 1(d)). In addition, the PCA analysis results in Figure 1(e) demonstrated that SCI could be distinguished before and after based on the degree of immune cell infiltration.

Further analysis was conducted by building a co-expression network using WGCNA to identify core genes significantly associated with disease phenotypes and gene expression in SCI. We analyzed the merged dataset of batch-corrected GSE180767 and GSE132242 and selected

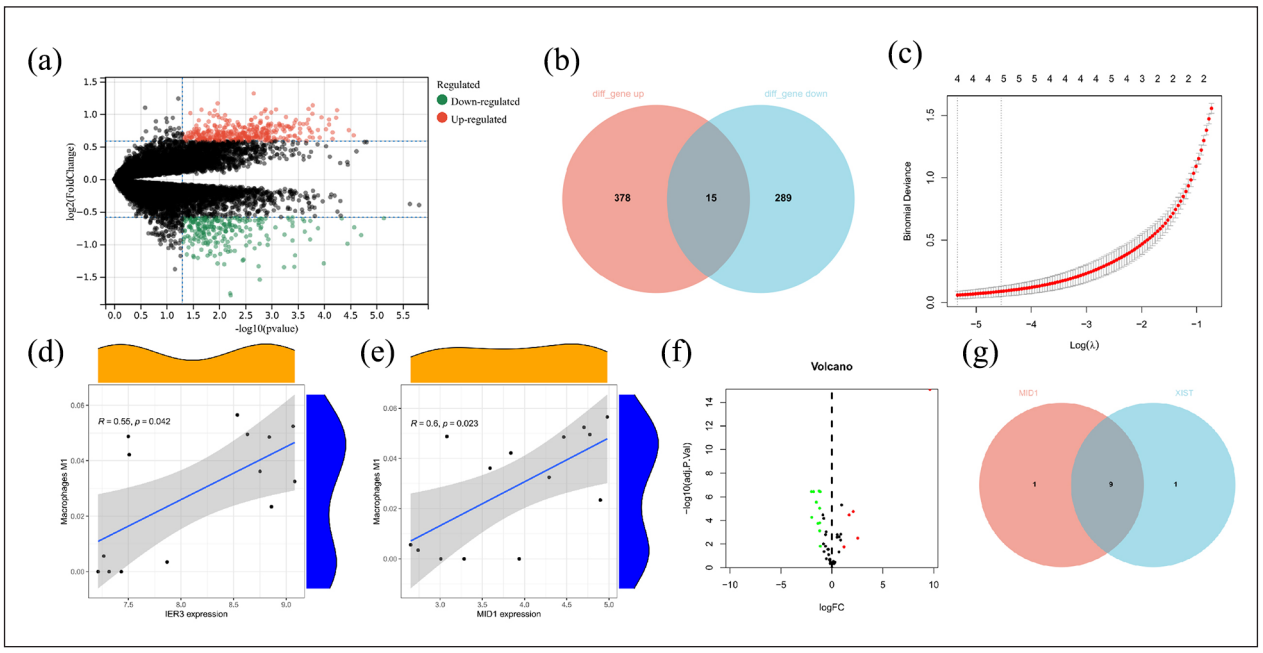

Figure 2. Bioinformatics analysis to screen key factors of BMSCs that regulate the polarization of M2-type macrophages.
(a) Volcano plot of differentially expressed genes in the combined dataset of AGSE139227 and GSE178564, red represents upregulation and green represents downregulation, (b) venn diagram of core genes up-regulated in the combined dataset of GSE180767 and GSE132242 versus differentially genes downregulated in the combined dataset of GSE139227 and GSE178564, (c) Cross-validation curves of LASSO genes, (d) correlation analysis of IER3 in GSE139227, GSE178564 combined dataset and M1 type macrophage infiltration, (e) correlation analysis of MID1 in GSE139227, GSE178564 combined dataset and M1 type macrophage infiltration, (f) GSE125176 dataset volcano plot of differential lncRNAs, red represents up-regulation, green represents down-regulation, and (g) venn diagram of binding proteins predicted by catRAPID website to interact with MID1, XISTRNA ranked in the top 10 tendencies.

a soft thresholding parameter β of 11 when using a correlation coefficient threshold of 0.9 (Figure 1(f)). Subsequently, we obtained five co-expression modules through WGCNA analysis (Figure 1(g)). The correlation analysis of module characteristics showed that the core genes in the magenta module were significantly negatively correlated with SCI, while the core genes in the brown module were significantly positively correlated with SCI (Figure 1(h)). Furthermore, by intersecting the genes in the brown module with the differential genes in the merged dataset, we obtained 453 core genes (Figure 1(i)).

We then performed a Gene Ontology (GO) analysis on the core genes obtained from the intersection of WGCNA and differential genes. The results showed that the core genes were mainly enriched in biological processes (BP), such as positive regulation of cytokine production, positive regulation of response to external stimulus, and wound healing. In cellular components (CC), they were mainly enriched in items such as collagen-containing extracellular matrix, external side of plasma membrane, and cytoplasmic vesicle lumen. In molecular function (MF), they were mainly enriched in items such as cytokine receptor binding, cytokine activity, and immune receptor activity (Supplemental Figure 1D). KEGG analysis revealed enrichment in signaling pathways such as Cytokine-cytokine receptor interaction, Osteoclast differentiation, TNF signaling pathway, Chemokine signaling pathway, and NF-kappa B signaling pathway (Supplemental Figure 1E).

LASSO machine algorithm screening yields XIST, a key factor (MID1) in the regulation of M2 macrophage polarization by BMSCs

To further screen the key factors of BMSCs for SCI, we performed a merge and difference analysis on the datasets GSE139227 and GSE178564 related to BMSCs transplantation for spinal cord injury. We obtained 872 different genes, of which 568 were up-regulated and 304 were down-regulated (Figure 2(a)). The up-regulated core genes in the combined dataset of GSE180767 and GSE132242 were intersected with the down-regulated differential genes in the combined dataset of GSE139227 and GSE178564 to obtain 15 core genes (Figure 2(b)). Subsequently, the 15 core genes were used to construct LASSO regression models by machine learning to obtain four core genes: SPHK1, IER3, MID1, and IGFBP2 (Figure 2(c)). We further analyzed the correlation between the f2 LASSO core genes and immune cells in the

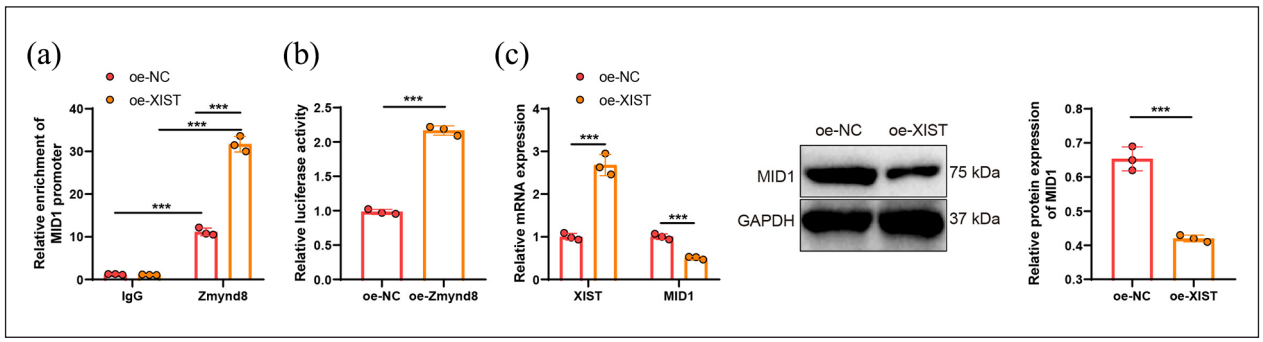

Figure 3. XIST promotes the enrichment of Zmynd8 into the promoter region of MID1.
(a) The ChIP experiment was conducted to determine the binding of Zmynd8 in the promoter region of MID1 in macrophages, (b) Dual-luciferase reporter assay was used to examine the transcriptional regulation of MID1 by Zmynd8 in macrophages, (c) qRT-PCR and Western blot analysis were performed to assess the expression of XIST and MID1 in macrophages, * indicates the comparison between two groups, $p < 0.05$, cell experiments were repeated at least three times.

combined dataset of GSE180767 and GSE132242. We showed that IER3 and MID1 were significantly associated with SCI-induced M1 polarization of macrophages (Figure 2(d) and (e)).

To clarify the specific mechanism by which BMSCs regulate macrophage polarization, we performed differential analysis on the BMSCs-related dataset GSE125176. We obtained 15 differential lncRNAs, of which 4 were up-regulated and 11 were down-regulated (Figure 2(f)). With the help of the catRAPID website, we found multiple identical binding proteins between XIST and the MID1 promoter, which contains a transcriptional regulator, Zmynd8 (Figure 2(g)).

XIST may enrich Zmynd8 into the promoter region of MID1 and thus repress MID1 transcription

The binding of Zmynd8 in the MID1 promoter region was examined using ChIP experiments (Figure 3(a)). The results demonstrated a significant increase in enrichment of the MID1 promoter fragment with Zmynd8 antibody immunoprecipitation compared to the IgG antibody group ($p < 0.05$). Additionally, overexpression of XIST was found to enhance the enrichment of Zmynd8 in the MID1 promoter. To investigate the relationship between Zmynd8 and MID1 in BMDM cells, simultaneous overexpression of MID1 promoter and empty vector or Zmynd8 was performed, and the dual-luciferase reporter system was employed. The results revealed a significant increase in luciferase activity in BMDM cells following Zmynd8 overexpression (Figure 3(b)).

Next, BMSCs overexpressing empty vector or XIST were co-cultured with BMDM cells, and qRT-PCR and WB analysis were conducted to evaluate the effects on BMDM cells. The results demonstrated that XIST overexpression significantly suppressed MID1 expression ($p < 0.05$; Figure 3(c)).

BMSCs-XIST induces macrophage M2 polarization in vitro and in vivo

To further investigate whether BMSCs-XIST can induce macrophage M2 polarization. In the first step, BMSCs were firstly identified by flow cytometry in cultured mice, and positive expression of CD90, CD73, CD105, and CD44 and negative expression of CD45 and CD31 were detected in BMSCs (Supplemental Figure 2A); in addition, lipogenic, osteogenic and chondrogenic differentiation was induced in MSCs, and BMSCs were shown to possess lipogenic, osteogenic, and BMSCs were shown to be capable of lipogenic, osteogenic, and chondrogenic differentiation (Supplemental Figure 2B).

Subsequently, we generated stable overexpressing BMSCs of XIST using lentivirus, named BMSCs-XIST, as well as control BMSCs expressing an empty vector. These two groups were co-cultured with BMDM, and the expression of XIST and MID1 in BMDM cells was examined using qRT-PCR. The results showed that compared to the BMSCs-NC group, the BMSCs-XIST group exhibited a significant increase in XIST expression and a significant decrease in MID1 expression in BMDM cells (Figure 4(a)).

To investigate whether BMSCs-XIST might affect the infiltrating macrophages in the injury area, we divided the experimental mice into four groups: Sham group, SCI group, BMSCs group, and BMSCs-XIST group, and detected the infiltration of macrophages in the injury area by RT-qPCR on the spinal cord tissues of mice, and the results showed that the spinal cord tissues of M1-type macrophage markers Nos2, Ccr7, and Cd86 were significantly increased in spinal cord tissues after SCI surgery; after administration of BMSCs and BMSCs-XIST treatment, the expression of M1-type macrophage markers was significantly decreased, while the expression of M2-type macrophage markers Arg1, Cd206, and Il-10 was significantly increased, with a more significant trend in the BMSCs-XIST group (Figure 4(a) and (c)). In addition,

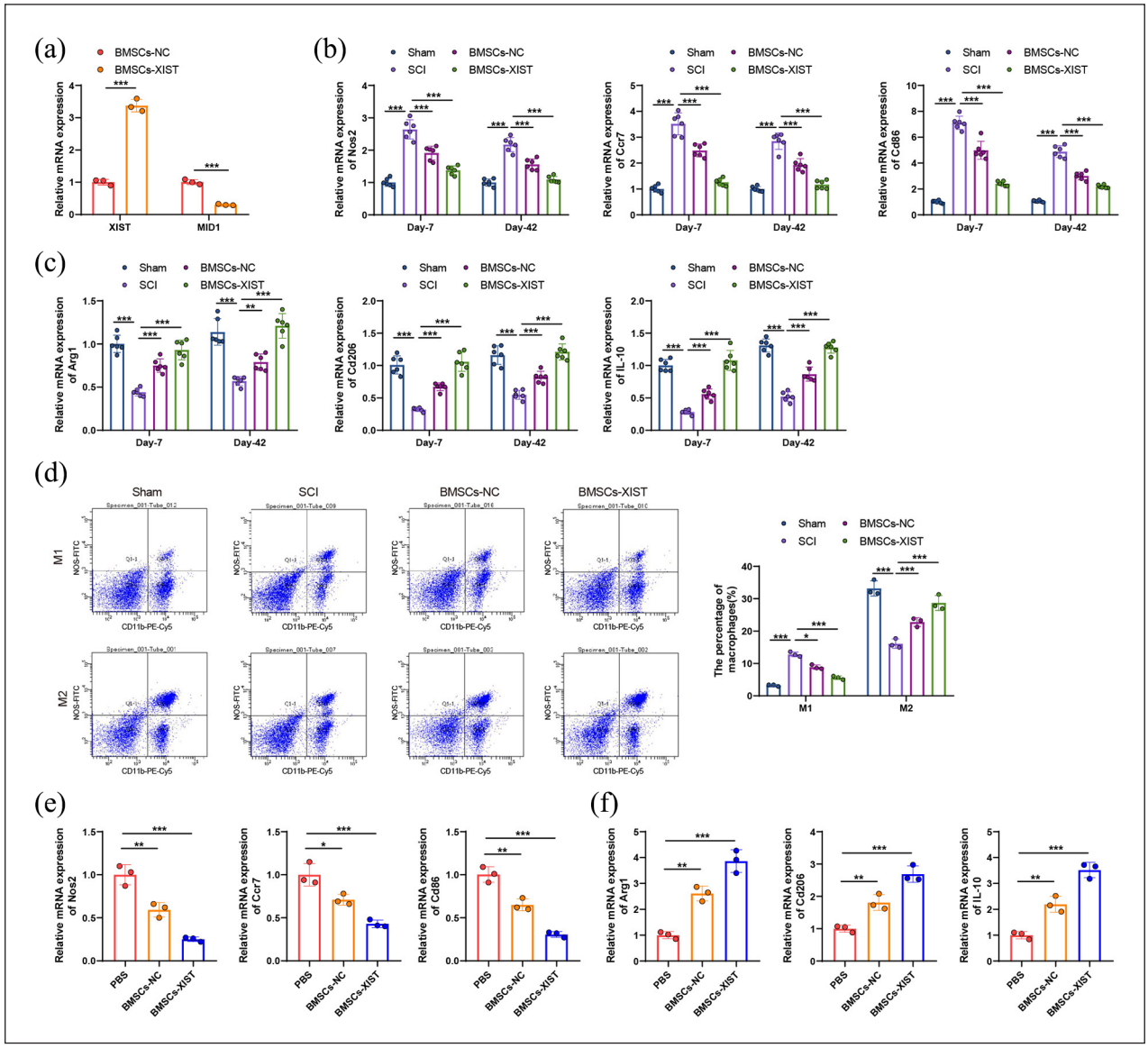

Figure 4. Effect of BMSCs-XIST on the polarization of M2-type macrophages.
(a) qRT-PCR assay to detect the expression of XIST and MID1 in BMDM infected with XIST lentivirus, (b and c) RT-qPCR to detect the gene expression levels of M1-type macrophage markers Nos2, Ccr7, and Cd86 and M2-type macrophage markers Arg1, Cd206, and Il-10 in the spinal cord tissues of each group of mice; (d) Flow cytometry to detect the ratio of M1 and M2 cells in the spinal cord tissue of each group of mice; (e and f) RT-qPCR to detect the gene expression levels of M1-type macrophage markers Nos2, Ccr7, and Cd86 and M2-type macrophage markers Arg1, Cd206, and Il-10 in each group of BMDM. Six mice per group, * indicates a comparison between two groups, $p < 0.05$, $^{**}p < 0.01$, $^{***}p < 0.001$, and cellular experiments were repeated at least three times.

flow cytometry detected the proportion of M1 and M2 cells in the spinal cord tissues of mice in each group, and the results showed that the proportion of M1 macrophages and the proportion of M2 macrophages in the spinal cord tissues increased significantly after SCI surgery; after the administration of BMSCs and BMSCs-XIST, the proportion of M1 macrophages decreased significantly, while the proportion of M2 macrophages increased significantly, with the BMSCs -XIST group showed a more significant trend (Figure 4(d)).

For further in vitro cell validation, we incubated BMSCs-XIST with BMDM. RT-qPCR results showed that compared with the PBS group, the M1-type macrophage marker levels were significantly decreased, and the M2-type macrophage marker expression levels were significantly increased in the BMSCs group and BMSCs-XIST group, with a more pronounced trend in the BMSCs-XIST group (Figure 4(e) and (f)).

BMSCs-XIST accelerates homeostatic microenvironment remodeling in NSCs by inducing M2-type macrophage polarization

Initially, NSCs were isolated from mouse spinal cord tissue and passaged three times. Immunofluorescent co-staining was performed for validation, demonstrating that

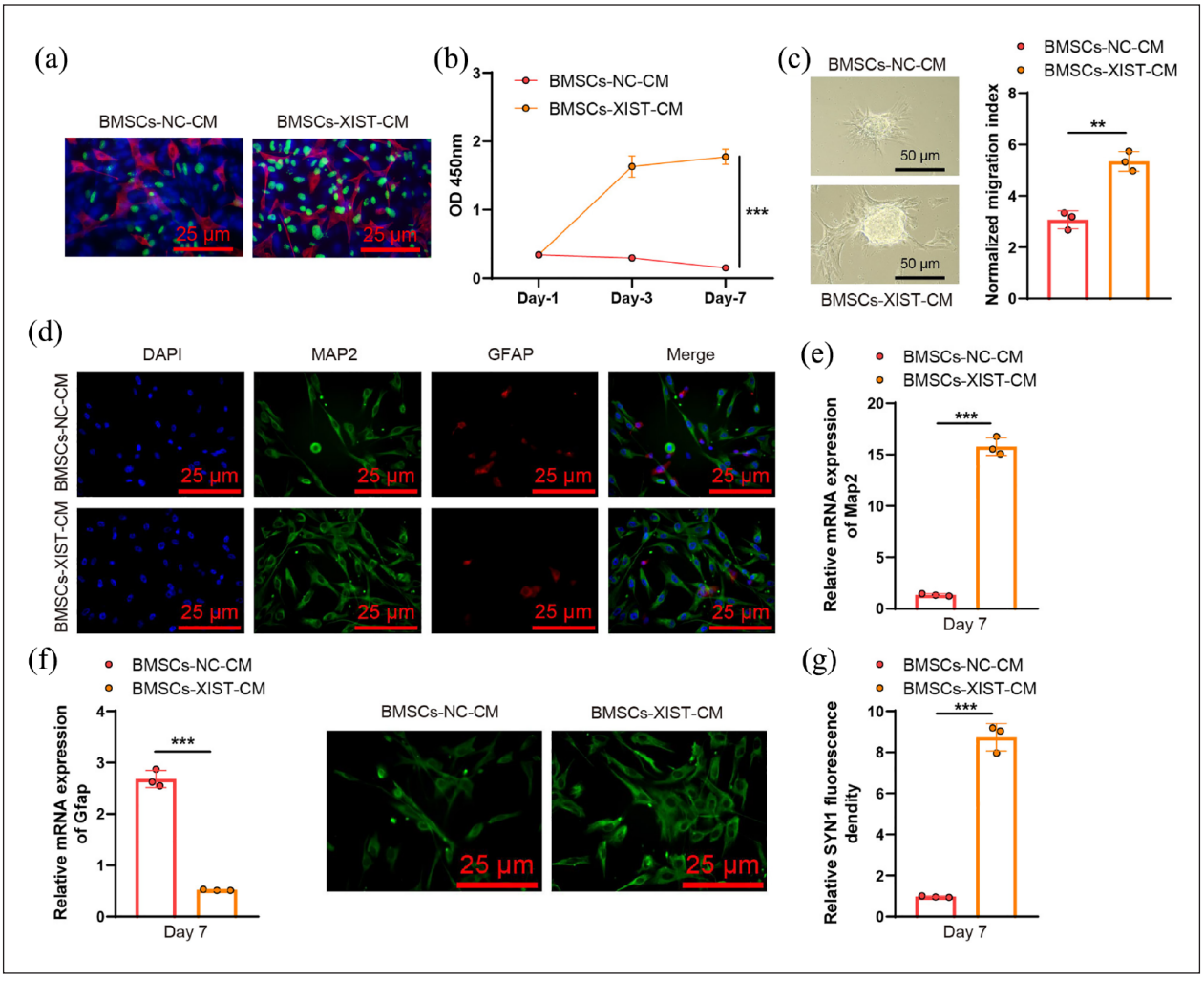

Figure 5. Effect of BMSCs-XIST on the microenvironment of NSCs.
(a) EdU staining to detect the proliferation of NSCs in each group, blue DAPI stained nuclei, red NESTIN stained NSCs, green EdU stained proliferating NSCs, scale bar = 25 μm, (b) CCK-8 to detect the proliferation of NSCs in each group, (c) detection of migration of NSCs in each group, for more visual observation of migration distance difference, (d) immunofluorescence co-staining for positive neuronal and astrocyte markers in each group of NSCs, scale bar = 25 μm; (eand f) RT-qPCR for gene expression levels of neuronal and astrocyte markers in each group of NSCs, and (g) immunofluorescence co-staining for neuronal axon formation in each group of NSCs (scale bar = 25 μm).
*Indicates the comparison between two groups, $p < 0.05$, and cell experiments were repeated at least three times.

over 90% of NSCs were positive for NESTIN and over 95% were positive for SOX2 (Supplemental Figure 3A-C).

NSCs proliferation and migration were assessed through CCK-8, EdU staining, and migration experiments. The results revealed that compared to CM from BMSCs-NC-treated BMDM, CM from BMSCs-XIST-treated BMDM significantly promoted NSCs proliferation and migration (Figure 5(a)–(c)). Furthermore, immunofluorescent co-staining and RT-qPCR were employed to examine neuronal (MAP2) and astrocyte (GFAP) markers. It was found that co-culturing BMSCs-XIST with BMDM significantly enhanced NSCs differentiation towards neurons, as evidenced by increased MAP2 expression, while inhibiting astrocyte differentiation, indicated by decreased GFAP expression (Figure 5(d)–(f)). RT-PCR analysis of inflammation-related factors in the NSCs steady-state microenvironment revealed that polarization of M2 macrophages increased the expression of anti-inflammatory factors (Supplemental Figure 4). Finally, the positive expression of SYN1 demonstrated that co-culturing BMSCs-XIST with BMDM promoted neuronal axon formation (Figure 5(g)).

NSCs proliferation and migration were assessed through CCK-8, EdU staining, and migration experiments. The results revealed that compared to CM from BMSCs-NC-treated BMDM, CM from BMSCs-XIST-treated BMDM significantly promoted NSCs proliferation and migration (Figure 5(a)–(c)). Furthermore,

immunofluorescent co-staining and RT-qPCR were employed to examine neuronal (MAP2) and astrocyte (GFAP) markers. It was found that co-culturing BMSCs-XIST with BMDM significantly enhanced NSCs differentiation towards neurons, as evidenced by increased MAP2 expression, while inhibiting astrocyte differentiation, indicated by decreased GFAP expression (Figure 5(d)–(f)). RT-PCR analysis of inflammation-related factors in the NSCs steady-state microenvironment revealed that polarization of M2 macrophages increased the expression of anti-inflammatory factors (Supplemental Figure 4). Finally, the positive expression of SYN1 demonstrated that co-culturing BMSCs-XIST with BMDM promoted neuronal axon formation (Figure 5(g)).

To directly demonstrate that it is M2-type macrophages that promote NSCs proliferation, migration, and differentiation toward neurons and axon formation, we directly cultured CMs of bone marrow macrophages (M0) and polarized M1 and M2 macrophages with NSCs and confirmed that it is M2-type macrophages, but not M0 and M1-type macrophages, that promote NSCs proliferation, migration, and differentiation toward neurons and axon formation (Supplemental Figure 5).

BMSCs-XIST promotes spinal cord repair in SCI mice by remodeling the homeostatic microenvironment of NSCs

Preoperative and postoperative mouse weights were recorded at 6 weeks. It was observed that the mouse weight increased in all groups at 6 weeks post-surgery. However, there was no significant difference in the mouse weight between the SCI, BMSCs-NC, and BMSCs-XIST groups, indicating that the treatment of BMSCs-NC and BMSCs-XIST did not cause any weight changes in SCI mice (Supplemental Figure 6).

Furthermore, at 6 weeks post-surgery, the levels of oxidative stress markers (T-AOC, T-SOD, CAT, and MDA activity) were measured in the spinal cord tissues of each group. The results (Supplemental Table 2) showed that compared to the Sham group, the SCI group exhibited significantly decreased T-AOC, T-SOD, and CAT activity, and significantly increased MDA activity. However, after treatment with BMSCs and BMSCs-XIST, there was a significant increase in T-AOC, T-SOD, and CAT activity, as well as a significant decrease in MDA activity, with the most significant changes observed in the BMSCs-XIST group. These findings suggest that BMSCs-XIST can alleviate spinal cord oxidative stress induced by SCI.

The Basso-mouse scale scored the motor behavior of mice. Figure 6(a) showed that all groups of mice showed normal motor behavior before the injury. After SCI surgery, the motor ability was significantly reduced. In contrast, after administering BMSCs and BMSCs-XIST treatment, the mice recovered their motor ability. The mice in the BMSCs-XIST group recovered. The best recovery was observed in the BMSCs-XIST group. In addition, the footprint distribution (Figure 6(b)), support base (Figure 6(c)), stride length (Figure 6(d)), and rotation angle (Figure 6(e)) of the mice were further summarized based on the footprint distribution of the hind limbs. And toe-dragging (Figure 6(f)). The data were used to assess limb coordination in mice, and the trend was consistent with Figure 5(a), showing that BMSCs-XIST significantly enhanced limb coordination in mice.

In addition, we investigated the effect of BMSCs-XIST on the expression of regeneration-associated genes (RAGs) during acute (7 days postoperatively) and chronic SCI (42 days postoperatively). These genes were selected from neurological development (GO: 0007399), motor recovery (GO: 0007626), and chemical synaptic transmission (GO: 0007268). RT-qPCR results showed that regeneration-related gene expression in spinal cord tissue was significantly reduced in both acute phases after SCI surgery. After administration of BMSCs and BMSCs-XIST treatment, In both the acute and chronic phases, the expression of these related genes increased significantly compared to the SCI group. The increase was more pronounced in the BMSCs-XIST group compared to the BMSCs group (Figure 6(g) and (h)).

At 6 weeks after surgery, spinal cord tissue was removed (Figure 7(a)), and H&E staining showed that compared with the Sham group, the SCI group mice had little regenerated tissue and larger cavity volume in the spinal cord. In addition, the damage score was significantly increased. After treatment with BMSCs and BMSCs-XIST, the regenerated tissue in the spinal cord of mice showed a linearly ordered structure with reduced cavity volume, and the damage score was The most significant changes were observed in BMSCs-XIST (Figure 7(b) and (d)). This result indicates that BMSCs-XIST can significantly promote spinal cord tissue regeneration. In addition, Masson staining showed that blue collagen deposition was significantly increased in spinal cord tissue after SCI surgery, while collagen deposition was significantly reduced in the BMSCs and BMSCs-XIST groups, with lower in the BMSCs-XIST group (Figure 7(c) and (e)). This finding suggests that BMSCs-XIST significantly reduces collagen deposition and may provide a suitable microenvironment for axonal regeneration.

Finally, the differentiation of NSCs in the spinal cord injury region was detected by immunofluorescence co-staining. We can see from Figure 7(f) that although MAP2-positive neurons and GFAP-positive astrocytes were seen at the injury site in all groups of mice in the SCI, BMSCs, and BMSCs-XIST groups, the BMSCs-XIST group mice

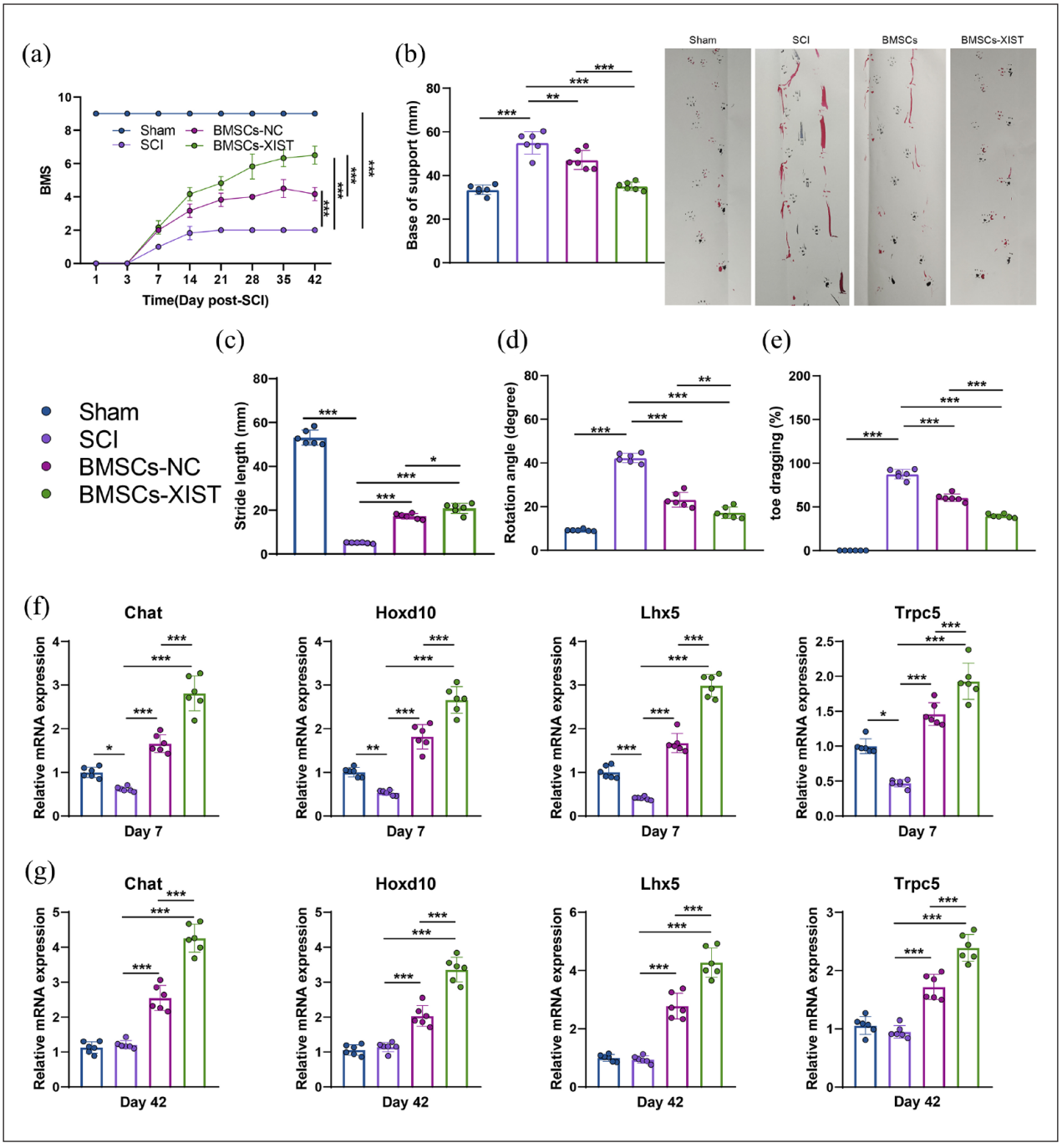

Figure 6. Effect of BMSCs-XIST on motor function in mice.
(a) BMS score to assess the motility of each group of mice, (b)–(e) day 42, footprint distribution, support, rotation angle, stride length, and toe drag distance of each group of mice, (f) RT-qPCR to detect the gene expression levels of tissue regeneration-related factors in each group of mice in the acute phase (7 d), (g) RT-qPCR to detect the gene expression levels of tissue regeneration-related factors in the chronic phase (42 d) The gene expression levels of tissue regeneration-related factors in each group of mice were measured by RT-qPCR. Six mice in each group, * indicates the comparison between two groups, $p < 0.05$, $^{**}p < 0.01$, $^{***}p < 0.001$.

had the highest neuron-positive The signal density was the highest in the BMSCs-XIST group, while GFAP-positive astrocytes were the lowest, followed by the BMSCs group. In addition, Western blot detection of MAP2 and GFAP expression in spinal cord tissue further confirmed the results of immunofluorescence co-staining (Figure 7(g)).

Discussion

First, bioinformatics analysis showed that BMSCs were transplanted with SCI in vitro, in which M2 macrophage infiltration was significantly increased and XIST may be a key factor regulating M2 macrophage polarization.

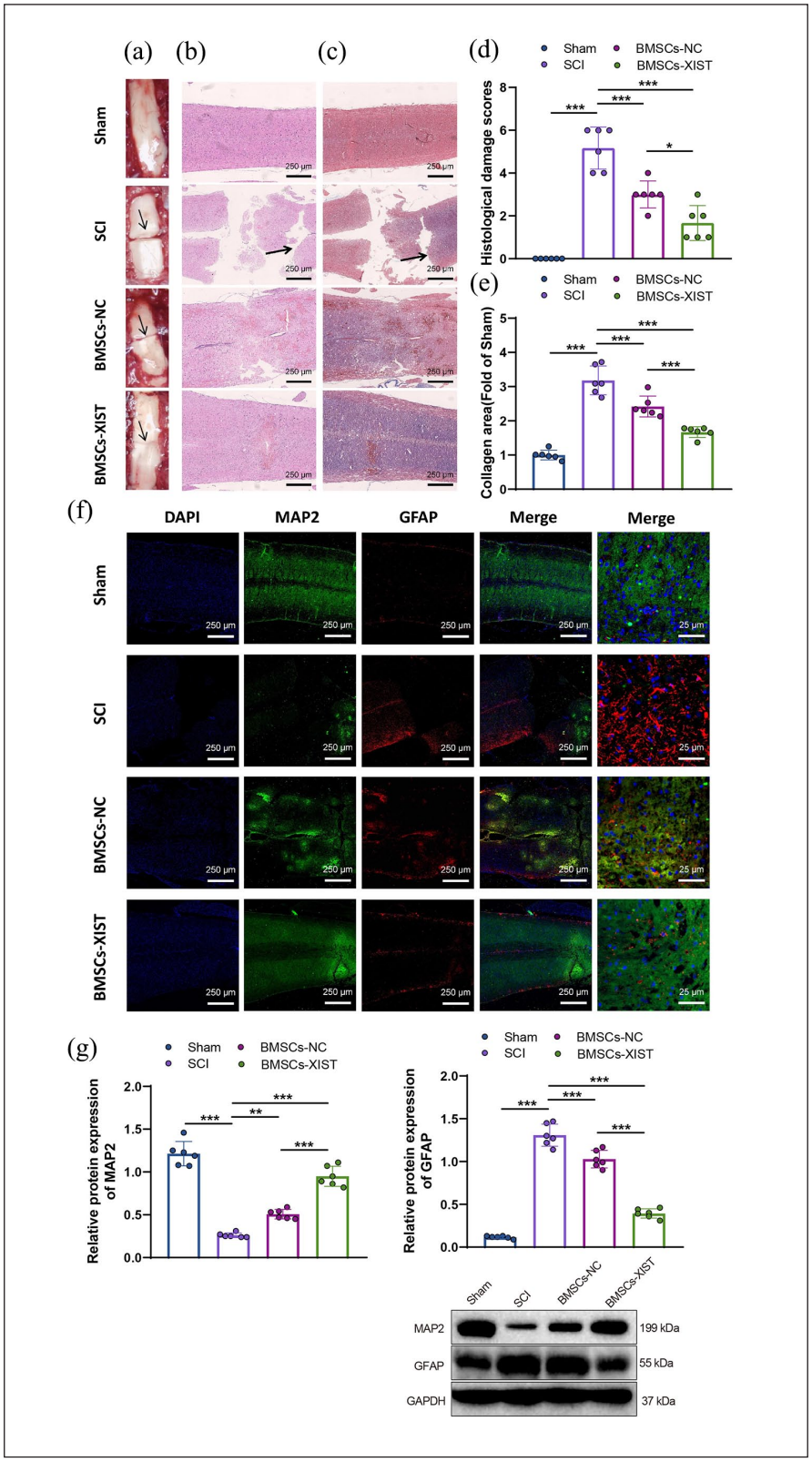

Figure 7. Effect of BMSCs-XIST on tissue healing, collagen deposition, and differentiation of NSCs in mouse spinal cord.
(a) White light map of spinal cord or spinal cord injury area in each group of mice (black arrow points to gel), (b) H&E staining to detect regeneration of spinal cord tissue in each group of mice (scale bar = 250 μm, black arrow points to the cavity), (c) Masson staining to detect collagen deposition in spinal cord tissue in each group of mice (scale bar = 250 μm, black arrow points to collagen deposition), (d) spinal cord injury score in Figure b, (e) collagen area in Figure c, (f) immunofluorescence co-staining for MAP2 and GFAP expression in spinal cord tissues of each group of mice (scale bar = 25 μm), and (g) Western blot for MAP2 and GFAP expression in spinal cord tissues of each group of mice. Six mice in each group, * indicates the comparison between two groups, $p < 0.05$, $^{**}p < 0.01$.

Subsequently, the expression of XIST in BMSCs was activated by CRISPR, and the results of in vitro experiments showed that BMSCs-XIST could induce macrophage M2 polarization. Furthermore, in vitro cell validation experiments confirmed that BMSCs-XIST could inhibit the inflammatory response and accelerate the reconstruction of the homeostatic microenvironment of NSCs by inducing macrophage M2 polarization, thus promoting NSCs proliferation, migration, differentiation, and axonal growth. Finally, in vivo, animal experiments confirmed that BMSCs-XIST could significantly alleviate SCI by promoting NSC differentiation and axon formation in the injured region.

Transplantation of BMSCs is considered a vital breakthrough point for SCI treatment.[44,45] Long-stranded non-coding RNAs were also found to play an essential role in the pathogenesis of SCI.[46,47] XIST plays a vital role in X chromosome silencing, regulating gene expression in multiple ways at the epigenetic, chromatin remodeling, transcriptional, and translational levels.[48] XIST Aberrant expression is associated with tumors, pulmonary fibrosis, inflammation, neuropathic pain, cardiomyocyte hypertrophy, and osteoarthritic chondrocytes.[48] XIST is up-regulated in models of spinal cord injury, and miR-219-5p analogs can inhibit XIST expression from reducing microglia damage after spinal cord injury.[46] A study by Zhao et al. reported that inhibiting the long non-coding RNA XIST aggravates spinal cord injury. Their research focused on directly assessing the effects of XIST in microglial cells, concluding that overexpressing XIST promotes the differentiation of microglial cells towards the M1 phenotype. In contrast, our study investigates the role of XIST in bone marrow stem cell therapy for spinal cord injury. We found that XIST can suppress the expression of the MID1 protein in bone marrow stem cells, promoting the differentiation of macrophages in the immune environment towards the M2 phenotype.

Furthermore, this facilitates the further differentiation of NSC cells towards the neuronal lineage, thereby facilitating spinal cord injury recovery. These findings align with previous reports that XIST promotes the polarization of macrophages toward the M2 phenotype.[17] In addition, silencing XIST was found to reduce the symptoms of cartilage injury in OA mice. Regarding the specific mechanism, XIST expression is downregulated during the differentiation of BMSCs into cartilage, and inhibition of FUT1 restores XIST expression levels and thus inhibits the differentiation of BMSCs.[49] Taken together, XIST may be an essential factor in the successful transplantation of BMSCs for SCI.

Increased polarization of M2-type macrophages can repair SCI and reduce neurological damage brought about by SCI.[50,51] A recent study found that MSCs-derived exosomes can promote the repair of traumatic spinal cord injury by altering microglia's M1/M2 polarization ratio, a type of macrophage in the brain.[52] It has also been found that XIST can promote the polarization of M2 macrophages.[17,53] For example, in a study of burn wound repair, XIST increased IL-33 expression levels by inhibiting miR-19b, promoted the proliferation and migration of skin fibroblasts, and promoted fibroblast extracellular matrix production by promoting the conversion of macrophages to the M2 phenotype.[17] However, no studies exist on XIST expression levels and macrophage polarization in BMSC.

It has been shown that miR-219-5p-mediated XIST silencing promotes microglia activity, inhibits apoptosis and inflammation, and thus promotes recovery from spinal cord injury.[46] It has also been found that XIST can promote the polarization of M2 macrophages.[17,53] For example, in a study of burn wound repair, XIST increased IL-33 expression levels by inhibiting miR-19b, promoted the proliferation and migration of skin fibroblasts, and promoted fibroblast extracellular matrix production by promoting the conversion of macrophages to the M2 phenotype.[17] Furthermore, in another study on neural stem cell transplantation to replenish neuronal deficits after spinal cord injury, M2-type macrophages were found to promote neural stem cell differentiation and, thus, neuronal cell formation by improving the inflammatory microenvironment.[54] However, no evidence exists that BMSCs can promote neural stem cell re-differentiation by regulating XIST. In contrast, our experiments can directly demonstrate that transplantation of BMSCs overexpressing XIST can reconstitute the microenvironment of neural stem cells by increasing the polarization of M2-type macrophages, providing a soil for neural stem cells to revalue, differentiate, and thus generate a sufficient amount of mature neurons to form synapses. Therefore, transplanting BMSCs-BDNF is expected to reactivate the neural stem cells in the SCI region and thus alleviate SCI.

Neural stem cells can differentiate into neurons, astrocytes, and oligodendrocytes, and these differentiated cells are more easily absorbed by spinal cord tissue and promote tissue injury repair, so neural stem cell transplantation is considered the most advantageous therapy,[55] and relevant clinical trials have already been approved.[56] However, chronic inflammation at the damaged site makes it often difficult for transplanted neural stem cells to survive and differentiate in a microenvironmental imbalance.[57,58] Our study found that BMSCs-XIST could improve the inflammatory microenvironment in the SCI region by activating M2-type macrophage polarization, creating favorable conditions for the value-added and differentiation of neural stem cells. Thus, our findings suggest that transplantation of BMSCs-BDNF may be a potential means of treating or alleviating SCI.

Based on extensive past research, bone marrow mesenchymal stem cells (BMSCs) have been considered promising candidates with clinical application potential as they

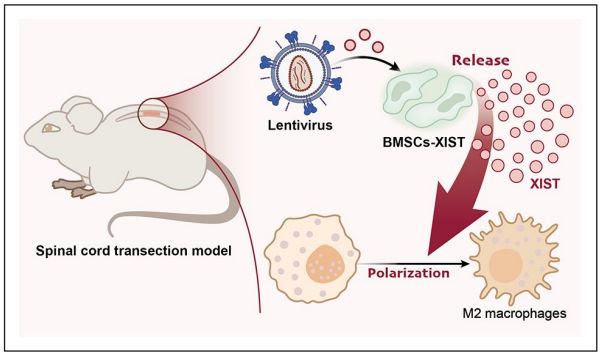

Figure 8. Molecular mechanism of XIST lentiviral overexpression vector modification of bone marrow mesenchymal stem cells to regulate macrophage polarization to affect the reconstruction of neural stem cell microenvironment in spinal cord injury.

have shown significant efficacy in repairing spinal cord injuries in experimental animal models. Furthermore, BMSCs are easily and safely applicable for autologous transplantation in clinical settings, and studies have indicated that direct transplantation of BMSCs into the lesion site contributes to improved axonal regeneration and motor function recovery in rats with spinal cord injuries.[59,60] Recently, it has been demonstrated that transplantation of lentivirus-mediated miR-28-5p-overexpressing BMSCs in rats with spinal cord injury effectively enhances neural recovery. This also suggests that miR-28-5p-modified BMSCs can serve as a therapeutic target to enhance behavioral and neural functional recovery in rats with spinal cord injuries.[61] Previous studies have also indicated that lentivirus-mediated miR-124-modified BMSC transplantation has a positive effect on spinal cord injury repair in rats.[62] In these studies and our own research, no specific safety concerns were identified regarding lentivirus-mediated overexpression vector-modified BMSCs. Due to time and budget limitations, we did not perform specific biochemical marker testing in this study. Further research and exploration are planned for the future.

In summary, we can conclude that BMSCs overexpressing XIST can accelerate the remodeling of the homeostatic microenvironment of NSCs by inhibiting MID1 transcription, inducing macrophage M2 polarization, suppressing the inflammatory response, and thus promoting NSCs proliferation and migration as well as differentiation to neurons and axonal growth, ultimately preventing SCI progression (Figure 8). Despite the many advantages of transplantation therapy for NSCs, transplantation of NSCs often dysregulates the microenvironment due to a chronic inflammatory response at the damaged site, which affects the survival and differentiation of transplanted NSCs.[57,58] Thus, we provide a new possible option for treating SCI from a theoretical point of view.

Conclusions

Nevertheless, there are still many unexplained aspects of our study. However, it is still unclear through which pathway XIST released by BMSCs activates M2 macrophage polarization, and this will be one of our future works. In addition, the immune cells infiltrating the SCI region are very diverse, and in addition to macrophages, there will be neutrophils and microglia.[58] The present study focuses on the effect of XIST on improving the speed of SCI recovery through the polarization of macrophages. The diversity of cellular interactions and communication mechanisms prevented us from determining whether XIST could also play a role in SCI repair by affecting the function of centrophils or microglia. Finally, from the perspective of clinical application, our study also only provides a theoretical possibility, and there is still a large amount of basic research needed to eventually realize the treatment of SCI by transplantation of BMSCs, as well as a multidisciplinary intersection to promote this technology for the ultimate benefit of SCI patients.

Author contributions

Dan Zhu, Tie Peng, Zhenwang Zhang, and Shuang Guo wrote the paper and conceived and designed the experiments; Ying Su and Kangwei Zhang analyzed the data; Jiawei Wang and Jiawei Wang collected and provided the sample for this study. All authors have read and approved the final submitted manuscript.

Availability of data and materials

The datasets used and analyzed during the current study are available from the corresponding author upon reasonable request.

Declaration of conflicting interests

The author(s) declared no potential conflicts of interest with respect to the research, authorship, and/or publication of this article.

Ethical approval

All animal experiments were approved by the Animal Ethics Committee of the Hubei University of Science and Technology (No. 2023-04-004). All animal experiments in this study followed the local management principles and the use of laboratory animals.

Funding

The author(s) disclosed receipt of the following financial support for the research, authorship, and/or publication of this article: This study was supported by Hubei University of Science and Technology "Medical Research Special Fund" (Grant Number 2022YKY18 to Dan Zhu), and Foundation of Hubei University of Science and Technology "Doctoral Initiation Fund" (Grant Number BK202414 to Dan Zhu), and Foundation of Hubei University of Science and Technology "Horizontal Research

Projects" (Grant Number 2023HX121 to Dan Zhu), and National Natural Science Foundation of China (Grant number 81870173 to Chao Liu), and "Special Project on Diabetes and Angiopathy" (Grant numbers 2022TNB01 Chao Liu).

ORCID iD

Chao Liu https://orcid.org/0009-0004-8789-5173

Supplemental material

Supplemental material for this article is available online.

References

1. Inoue K. A state-of-the-art perspective on microgliopathic pain. *Open Biol* 2018; 8: 180154.
2. Wang X, Wang SS, Huang H, et al. Effect of capecitabine maintenance therapy using lower dosage and higher frequency vs observation on disease-free survival among patients with early-stage triple-negative breast cancer who had received standard treatment: the SYSUCC-001 randomized clinical trial. *JAMA* 2021; 325: 50–58.
3. Fan L, Liu C, Chen X, et al. Exosomes-loaded electroconductive hydrogel synergistically promotes tissue repair after spinal cord injury via immunoregulation and enhancement of myelinated axon growth. *Adv Sci* 2022; 9: e2105586.
4. Zahorec R. Neutrophil-to-lymphocyte ratio, past, present and future perspectives. *Bratisl Lek Listy* 2021; 122: 474–488.
5. Xia Y, Yang R, Wang H, et al. Biomaterials delivery strategies to repair spinal cord injury by modulating macrophage phenotypes. *J Tissue Eng* 2022; 13: 20417314221143059.
6. Hong JY, Kim SH, Seo Y, et al. Self-assembling peptide gels promote angiogenesis and functional recovery after spinal cord injury in rats. *J Tissue Eng* 2022; 13: 20417314221086491.
7. Kofman S, Mohan N, Sun X, et al. Human mini brains and spinal cords in a dish: modeling strategies, current challenges, and prospective advances. *J Tissue Eng* 2022; 13: 20417314221113391.
8. Chen S and Shen X. Long noncoding RNAs: functions and mechanisms in colon cancer. *Mol Cancer* 2020; 19: 167.
9. Liu XY, Guo JW, Kou JQ, et al. Repair mechanism of astrocytes and non-astrocytes in spinal cord injury. *World J Clin Cases* 2020; 8: 854–863.
10. Zhao Q, Lu F, Su Q, et al. Knockdown of long noncoding RNA XIST mitigates the apoptosis and inflammatory injury of microglia cells after spinal cord injury through miR-27a/Smurf1 axis. *Neurosci Lett* 2020; 715: 134649.
11. Zhu G, Xia Y, Zhao Z, et al. LncRNA XIST from the bone marrow mesenchymal stem cell derived exosome promotes osteosarcoma growth and metastasis through miR-655/ACLY signal. *Cancer Cell Int* 2022; 22: 330.
12. Yang X, Zhang S, He C, et al. METTL14 suppresses proliferation and metastasis of colorectal cancer by down-regulating oncogenic long non-coding RNA XIST. *Mol Cancer* 2020; 19: 46.
13. Ziv Y and Schwartz M. Orchestrating brain-cell renewal: the role of immune cells in adult neurogenesis in health and disease. *Trends Mol Med* 2008; 14: 471–478.
14. Song H, Xu Y, Chang W, et al. Negative pressure wound therapy promotes wound healing by suppressing macrophage inflammation in diabetic ulcers. *Regen Med* 2020; 15: 2341–2349.
15. Kobashi S, Terashima T, Katagi M, et al. Transplantation of M2-deviated microglia promotes recovery of motor function after spinal cord injury in mice. *Mol Ther* 2020; 28: 254–265.
16. Li L, Lv G, Wang B, et al. XIST/miR-376c-5p/OPN axis modulates the influence of proinflammatory M1 macrophages on osteoarthritis chondrocyte apoptosis. *J Cell Physiol* 2020; 235: 281–293.
17. Pi L, Fang B, Meng X, et al. LncRNA XIST accelerates burn wound healing by promoting M2 macrophage polarization through targeting IL-33 via miR-19b. *Cell Death Discov* 2022; 8: 220.
18. Wan J and Liu B. Construction of lncRNA-related ceRNA regulatory network in diabetic subdermal endothelial cells. *Bioengineered* 2021; 12: 2592–2602.
19. Zhao Y, Wang L, Wu Y, et al. Genome-wide study of key genes and scoring system as potential noninvasive biomarkers for detection of suicide behavior in major depression disorder. *Bioengineered* 2020; 11: 1189–1196.
20. Li T, Wang W, Gan W, et al. Comprehensive bioinformatics analysis identifies LAPTM5 as a potential blood biomarker for hypertensive patients with left ventricular hypertrophy. *Aging* 2022; 14: 1508–1528.
21. Butler A, Hoffman P, Smibert P, et al. Integrating single-cell transcriptomic data across different conditions, technologies, and species. *Nat Biotechnol* 2018; 36: 411–420.
22. Mistry P, Nakabo S, O'Neil L, et al. Transcriptomic, epigenetic, and functional analyses implicate neutrophil diversity in the pathogenesis of systemic lupus erythematosus. *Proc Natl Acad Sci USA* 2019; 116: 25222–25228.
23. Yu G, Wang LG, Han Y, et al. ClusterProfiler: an R package for comparing biological themes among gene clusters. *OMICS* 2012; 16: 284–287.
24. Li J, Liu C, Chen Y, et al. Tumor characterization in breast cancer identifies immune-relevant gene signatures associated with prognosis. *Front Genet* 2019; 10: 1119.
25. Jin J, Ou Q, Wang Z, et al. BMSC-derived extracellular vesicles intervened the pathogenic changes of scleroderma in mice through miRNAs. *Stem Cell Res Ther* 2021; 12: 327.
26. Xue F, Wu J, Feng W, et al. MicroRNA-141 inhibits the differentiation of bone marrow-derived mesenchymal stem cells in steroid-induced osteonecrosis via E2F3. *Mol Med Rep* 2022; 26: 1–8.
27. Yang Y, Fan Y, Zhang H, et al. Small molecules combined with collagen hydrogel direct neurogenesis and migration of neural stem cells after spinal cord injury. *Biomaterials* 2021; 269: 120479.
28. Cho DI, Kim MR, Jeong HY, et al. Mesenchymal stem cells reciprocally regulate the M1/M2 balance in mouse bone marrow-derived macrophages. *Exp Mol Med* 2014; 46: e70.
29. Zhang K, Zheng J, Bian G, et al. Polarized macrophages have distinct roles in the differentiation and migration of embryonic spinal-cord-derived neural stem cells after grafting to injured sites of spinal cord. *Mol Ther* 2015; 23: 1077–1091.
30. Chen X, Wan Z, Yang L, et al. Exosomes derived from reparative M2-like macrophages prevent bone loss in murine periodontitis models via IL-10 mRNA. *J Nanobiotechnology* 2022; 20: 110.

31. Fan L, Liu C, Chen X, et al. Directing induced pluripotent stem cell derived neural stem cell fate with a three-dimensional biomimetic hydrogel for spinal cord injury repair. *ACS Appl Mater Interfaces* 2018; 10: 17742–17755.
32. Xu Y, Zhou J, Liu C, et al. Understanding the role of tissue-specific decellularized spinal cord matrix hydrogel for neural stem/progenitor cell microenvironment reconstruction and spinal cord injury. *Biomaterials* 2021; 268: 120596.
33. Luo F, Wang J, Zhang Z, et al. Inhibition of CSPG receptor PTPsigma promotes migration of newly born neuroblasts, axonal sprouting, and recovery from stroke. *Cell Rep* 2022; 40: 111137.
34. Zhan J, Li X, Luo D, et al. Polydatin promotes the neuronal differentiation of bone marrow mesenchymal stem cells in vitro and in vivo: Involvement of Nrf2 signalling pathway. *J Cell Mol Med* 2020; 24: 5317–5329.
35. Irrera N, Arcoraci V, Mannino F, et al. Activation of A2A receptor by PDRN reduces neuronal damage and stimulates WNT/beta-CATENIN driven neurogenesis in spinal cord injury. *Front Pharmacol* 2018; 9: 506.
36. Harada T, Tsuboi I, Hino H, et al. Age-related exacerbation of hematopoietic organ damage induced by systemic hyper-inflammation in senescence-accelerated mice. *Sci Rep* 2021; 11: 23250.
37. Chakravarthi B, Chandrashekar DS, Agarwal S, et al. MiR-34a regulates expression of the stathmin-1 oncoprotein and prostate cancer progression. *Mol Cancer Res* 2018; 16: 1125–1137.
38. Song C and Zhou C. HOXA10 mediates epithelial-mesenchymal transition to promote gastric cancer metastasis partly via modulation of TGFB2/Smad/METTL3 signaling axis. *J Exp Clin Cancer Res* 2021; 40: 62.
39. Yang Q, Guo XP, Cheng YL, et al. MicroRNA-143-5p targeting eEF2 gene mediates intervertebral disc degeneration through the AMPK signaling pathway. *Arthritis Res Ther* 2019; 21: 97.
40. Garikipati VNS, Verma SK, Cheng Z, et al. Circular RNA CircFndc3b modulates cardiac repair after myocardial infarction via FUS/VEGF-A axis. *Nat Commun* 2019; 10: 4317.
41. Ayuk SM, Abrahamse H and Houreld NN. The role of photobiomodulation on gene expression of cell adhesion molecules in diabetic wounded fibroblasts in vitro. *J Photochem Photobiol B* 2016; 161: 368–374.
42. Wu Q and Yi X. Down-regulation of long noncoding RNA MALAT1 protects hippocampal neurons against excessive autophagy and apoptosis via the PI3K/Akt signaling pathway in rats with epilepsy. *J Mol Neurosci* 2018; 65: 234–245.
43. Ma S, Mangala LS, Hu W, et al. CD63-mediated cloaking of VEGF in small extracellular vesicles contributes to anti-VEGF therapy resistance. *Cell Rep* 2021; 36: 109549.
44. Brock JH, Graham L, Staufenberg E, et al. Bone marrow stromal cell intraspinal transplants fail to improve motor outcomes in a severe model of spinal cord injury. *J Neurotrauma* 2016; 33: 1103–1114.
45. Andrzejewska A, Dabrowska S, Lukomska B, et al. Mesenchymal stem cells for neurological disorders. *Adv Sci* 2021; 8: 2002944.
46. Zhong X, Bao Y, Wu Q, et al. Long noncoding RNA XIST knockdown relieves the injury of microglia cells after spinal cord injury by sponging miR-219-5p. *Open Med* 2021; 16: 1090–1100.
47. Ding Y, Song Z and Liu J. Aberrant LncRNA expression profile in a contusion spinal cord injury mouse model. *Biomed Res Int* 2016; 2016: 9249401.
48. Wang W, Min L, Qiu X, et al. Biological function of long non-coding RNA (LncRNA) xist. *Front Cell Dev Biol* 2021; 9: 645647.
49. He JY, Cheng M, Ye JL, et al. YY1-induced lncRNA XIST inhibits cartilage differentiation of BMSCs by binding with TAF15 to stabilizing FUT1 expression. *Regen Ther* 2022; 20: 41–50.
50. Gaojian T, Dingfei Q, Linwei L, et al. Parthenolide promotes the repair of spinal cord injury by modulating M1/M2 polarization via the NF-kappaB and STAT 1/3 signaling pathway. *Cell Death Discov* 2020; 6: 97.
51. Li R, Zhao K, Ruan Q, et al. Bone marrow mesenchymal stem cell-derived exosomal microRNA-124-3p attenuates neurological damage in spinal cord ischemia-reperfusion injury by downregulating Ern1 and promoting M2 macrophage polarization. *Arthritis Res Ther* 2020; 22: 75.
52. Liu W, Rong Y, Wang J, et al. Exosome-shuttled miR-216a-5p from hypoxic preconditioned mesenchymal stem cells repair traumatic spinal cord injury by shifting microglial M1/M2 polarization. *J Neuroinflammation* 2020; 17: 47.
53. Sun Y and Xu J. TCF-4 regulated lncRNA-XIST promotes M2 polarization of macrophages and is associated with lung cancer. *Onco Targets Ther* 2019; 12: 8055–8062.
54. Zhang K, Lu WC, Zhang M, et al. Reducing host aldose reductase activity promotes neuronal differentiation of transplanted neural stem cells at spinal cord injury sites and facilitates locomotion recovery. *Neural Regen Res* 2022; 17: 1814–1820.
55. Lu P, Kadoya K and Tuszynski MH. Axonal growth and connectivity from neural stem cell grafts in models of spinal cord injury. *Curr Opin Neurobiol* 2014; 27: 103–109.
56. Curtis E, Martin JR, Gabel B, et al. A first-in-human, phase I study of neural stem cell transplantation for chronic spinal cord injury. *Cell Stem Cell* 2018; 22: 941–950 e946.
57. Fan B, Wei Z, Yao X, et al. Microenvironment imbalance of spinal cord injury. *Cell Transplant* 2018; 27: 853–866.
58. Orr MB and Gensel JC. Spinal cord injury scarring and inflammation: therapies targeting glial and inflammatory responses. *Neurotherapeutics* 2018; 15: 541–553.
59. Nakano N, Nakai Y, Seo TB, et al. Effects of bone marrow stromal cell transplantation through CSF on the subacute and chronic spinal cord injury in rats. *PLoS ONE* 2013; 8: e73494.
60. Himes BT, Neuhuber B, Coleman C, et al. Recovery of function following grafting of human bone marrow-derived stromal cells into the injured spinal cord. *Neurorehabil Neural Repair* 2006; 20: 278–296.
61. Li Z, Su H, Lin G, et al. Transplantation of MiR-28-5p-Modified BMSCs promotes functional recovery after spinal cord injury. *Mol Neurobiol* 2023; 21.
62. Song JL, Zheng W, Chen W, et al. Lentivirus-mediated microRNA-124 gene-modified bone marrow mesenchymal stem cell transplantation promotes the repair of spinal cord injury in rats. *Exp Mol Med* 2017; 49: e332.